Available online at www.sciencedirect.com
ScienceDirect
Catalysis Today 128 (2007) 88–99
CATALYSIS TODAY
www.elsevier.com/locate/cattod

Effects of pore assembly architecture on catalyst particle tortuosity and reaction effectiveness

S. Prachayawarakorn, R. Mann *

School of Chemical Engineering and Analytical Science, The University of Manchester, Manchester M60 1QD, UK

Abstract

The chaotic and random porosity of typical catalyst particles continues to present a challenge of quantification. An analysis is presented of the variation of diffusion and reaction performance with catalyst porosity architecture. The analysis uses simple 2D pore networks with O(10^3) pores. The impact of different pore assemblies is assessed for the special case of a bimodal distribution with equal numbers of micro- and macro-pores. A random pore assembly gives higher tortuosity values than the baseline unity tortuosity parallel bundle with identical surface reactivity, diffusivity, pore volume and specific surface. Improvements in particle reactivity are demonstrated for four illustrative porosity architectures—minimum shielding, partial cruciform, fully cruciform and fractal tree. Each of these assembled structures is more reactive than the random network when diffusional resistances intrude. The best reactivity is for the minimum shielding assembly, being some 800% better than random pores at a Thiele modulus of 1. Improved diffusional fluxes through the larger macro-pores, when they inter-penetrate effectively amongst the smaller pores, explains the improvements predicted. Details of the improvements can be discerned from colour-coded pore environmental plots. The practical potential for designing and subsequently fabricating optimal pore structures should be realised by extending to 3D models for porosity.

Keywords: Diffusion; Catalytic reaction; Porosity; Tortuosity; Pore size distribution; Effectiveness factor; Pore architecture

1. Introduction

Catalysis is at the heart of chemical manufacturing by virtue of the spectacular improvements in reaction rates and chemical selectivity that catalytic agents can provide. Fixed beds of catalyst particles are the predominant chemical reactor configuration because the particles are stationary leading to much-less attrition and particle damage than for fluidised and moving bed variants. Inevitably the catalytic agent, together with a support and promoters, need to be fabricated into particles which will both form a bed with an appropriate intra-bed porosity between the particles as well as an intra-particle porosity that facilitates the internal diffusion and catalytic reaction processes. Wide varieties of particle geometry are used seeking to secure intimate flow contacting coupled to good interstitial flow distribution and an acceptably low pressure drop. Particles are typically of millimetre dimensions.

Once a suitable particle geometry is selected, the particle interior porosity (ε_p) needs to be specified. With typical porosities ranging from 0.3 to 0.7, the particle interior properties are often defined by the macroscopic values of specific pore volume (V_p) and specific surface area (S_g), although either of these are sometimes implicit if a bulk density is also quoted. The values of the macroscopic pore volume and surface area typically indicate internal pore ‘‘spaces’’ of relatively very small dimensions. Thus although these values will depend on the geometry of the ‘‘spaces’’, for surface areas of several hundred $m^2\ g^{-1}$, the pore ‘‘spaces’’ will be of the order of nanometres. Even so-called low surface area catalysts with specific surface of around a few $m^2\ g^{-1}$ will consist mainly of pores of the order of microns (thus some two orders of magnitude less than the diameter of a human hair).

The internal porosity is readily imaged by scanning electron microscopy (SEM) and a typical view is shown in Fig. 1 for a fractured nickel–alumina particle from a sample of an industrial reforming catalyst. Inspection of Fig. 1 shows that the porosity appears to form a tangled mass of inter-connecting void ‘‘spaces’’ arising randomly in the fractured section. Moreover

---

* Corresponding author. Tel.: +44 161 306 4378; fax: +44 161 306 4399.
E-mail address: r.mann@manchester.ac.uk (R. Mann).

0920-5861/$ – see front matter © 2007 Elsevier B.V. All rights reserved.
doi:10.1016/j.cattod.2007.06.036

Nomenclature

C	concentration
D	molecular diffusivity
D_e	effective diffusivity
k_s	surface reaction rate constant
L	network (particle) length
m'	diffusion reaction parameter $(=(2\,k_s/rD_e)^{1/2})$
m	diffusion reaction parameter $(=(2\,k_s/r\mathrm{D})^{1/2})$
r	pore radius
S_g	specific surface
V_p	pore volume
ε_p	particle porosity
η	effectiveness factor
Φ	Thiele modulus
τ	tortuosity factor

the size, shape and texture of the void edges/surfaces likewise appear randomly rough, hugely irregular, wholly chaotic and unstructured in every conceivable sense. One might suppose by visual inspection that the average pore is of the order of one micron in ‘‘size’’, although there is evidently a huge variation from several microns down to less than one-tenth of a micron even without including invisible pores below the scale of scrutiny in Fig. 1. Clearly the task of describing and consequently quantifying the porosity evident in Fig. 1, in order to understand the interactions between pore structure and internal diffusional fluxes, presents something of a challenge to chemical reaction engineering for applied catalysis.

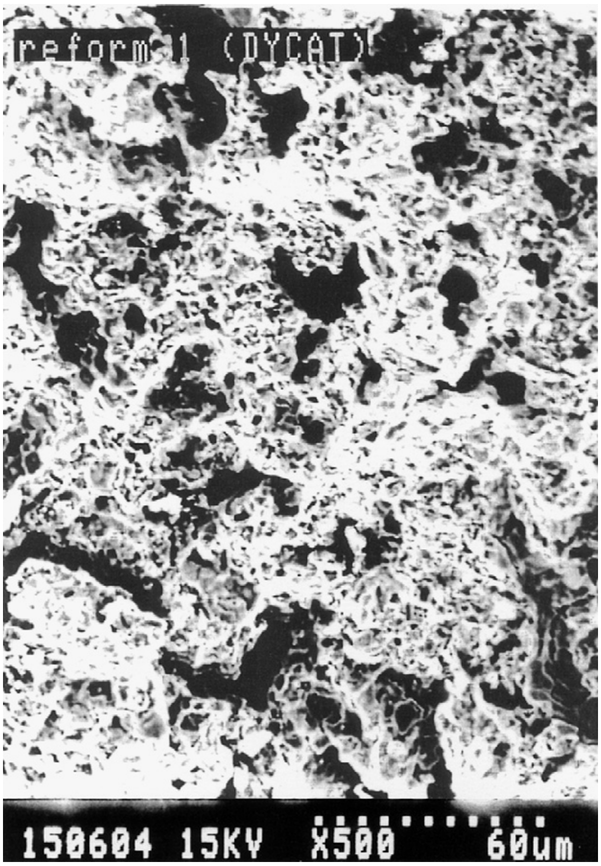

Fig. 1. Typical SEM image of catalyst particle interior porosity.

2. Empirical approaches via a tortuosity factor

The most popular approach to linking porosity complexity to intra-particle diffusional behaviour is via the so-called tortuosity factor. Thus for a sample of a porous material an effective diffusivity is defined [1,2] so that:

$$D_e = \left(\frac{\varepsilon_p}{\tau}\right) D \tag{1}$$

Here the effective diffusivity is made proportional to the actual diffusivity in the pore voids reduced by the porosity ε_p (this is the factor by which the pore space is not available because it is occupied by the solid) and further reduced by the tortuosity factor τ. This factor popularly accounts for the fact that the pore spaces do not provide straight-line paths through the particle (they are tortuous) thereby lengthening the diffusive path and reducing the driving gradient of any concentration difference. In most cases this factor is also used to additionally incorporate the effect of pore constrictions introduced because the pore voids inevitably vary in cross section [1–4], although some texts introduce an additional separate pore constriction factor [5]. Many classic texts refer directly or indirectly to the obvious inadequacies of this empirical approach, so that tortuosity is widely recognised to be ‘‘a plausible fudge factor’’ [2], although some recent texts fail to provide any mention of this difficult to quantify characteristic of catalyst performance [6,7].

3. Porosity features affecting tortuosity

Fig. 2 shows how the widely used idealised single pore model [8] which is straight, perfectly cylindrical and with a smooth surface compares with a schematic re-creation of a typical pore envisaged as being contained within a catalytic porous solid like that shown in Fig. 1. The first point to note is that this is a representative image of a typical pore, so that all pores will be expected to be individually different with several degrees of randomness according to the type of variability portrayed in Fig. 2.

The variable differences for each ‘‘pore’’ will be:

- length;
- non-straight (tortuous and sinuous);
- non-parallel sided;
- non-circular with irregular cross section;
- inter-connecting with variable connectivity;
- non-smooth walled with a randomly roughened surface (possibly fractal in nature).

Each of these factors needs to be quantitatively incorporated into a geometrically rigorous description suitable for predicting the diffusive fluxes (hence the tortuosity value). Such a capability would then facilitate the design of efficient pore

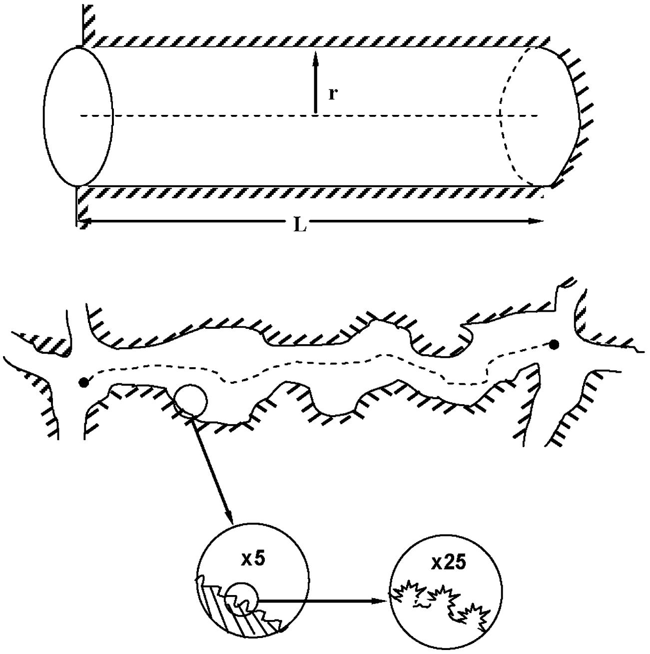

Fig. 2. Real pores compared with idealised model pore.

architectures from sound first principles. It has been suggested that that surface roughness can be accounted for by "the land surveyors approximation" [9], but this would be to ignore the important issue of the fractal character of surfaces under different magnifications [10,11].

4. Pore structure design

4.1. Empirical approaches by cut and try/hit and miss

Due to the lack of a fundamental framework for understanding the diffusion and reaction behaviour within typically complex geometry porosity, some approaches experimentally vary the balance of support and active catalytic component in searching out formulations with improved reactivity. See for example, variation of the silica/binder proportions in Fischer–Tropsch iron catalysts [12] and the impact of meso-pore size variation on platinum dispersion [13]. Even quite recently, optimisation for a silica supported V–Mg–O uses such an empirical non-model based approach [14].

4.2. Porosity design from sound fundamentals

Moves from qualitative to quantitative understanding can provide evidence that strengthens the motivation to create fully quantitative models. An interesting example of this was an appreciation of the need for more uniform porosity adsorbents in order to improve heavy metal adsorption in pollution control. Unlike the conventional amorphous silica-gel, the creation of well defined large diameter channels in the modified porous adsorbent precluded pore blockage by the grafting spheres whilst facilitating the access of heavy metal ions to the inter-gallery adsorption sites [15].

In applied catalysis, there are additional complications over and above basic catalytic reactivity. These include multi-component transport, reaction selectivity, resistance to deactivation and ease of regeneration. Covering this level of processing complexity requires the ultimate development of detailed porosity descriptions. These need to incorporate most if not all the key elements of physico-chemical behaviour, to enable design of catalyst particle pore size distribution and pore architecture based on fundamentals.

4.3. Models for porosity

In advancing beyond the single size idealised pore model in Fig. 2, assembly into networks of simple pores allows for variations in pore size distribution as well as inter-connectivity between pores. Combinations of distributed pore sizes (diameters) and their assembly architecture can be readily assessed quantitatively in 2D or more realistically in 3D. Network pore models have proved popular and have been progressively applied to a variety of problems relating to catalyst particles since their initial introduction in 2D for mercury porosimetry [16]. Amongst the more important cases are: interpretation of porosimetry in 3D [17]; extension to diffusion and reaction in 2D [18] and 3D [19,20]; and the resolving of pore structure through combining porosimetry and nitrogen adsorption [21]. Further developments included multi-component diffusion with reaction [22–24] in turn extended to also include simultaneous capillary condensation [25]. At an even greater level of complexity, pore networks have been applied to examine catalyst porosity changes induced by coke laydown in hydrocarbon catalysis [26]. Related developments have incorporated percolation concepts [27].

Whilst pore networks have been widely adopted other approaches are possible. Thus the closely related idea, whereby the pores are quantified as voids created amongst randomly assembled spheres, has also been pursued to good effect in quantifying catalyst particle porosity and tortuosity [28,29].

5. Design of porosity architecture

Most of the above work has focused on the reaction effectiveness of catalyst particles with "given" pore size distributions. However, the geometrical pore architecture, which is defined in terms of the ways a given set of pore segments may be assembled, is possibly also important as well. This resolves to the question of "design" of the pore architecture assembly for a given set of pores possessing a given pore size distribution. The role of inter-connectivity in optimizing a pore network model for a hydrodemetallation catalyst has been explored [30]. Also recently, Gheorgiu and Coppens [31] have specifically explored the closely related issue of pore structure optimisation over a large range of scales of pore size. They have shown that a broad pore size distribution can be made close to optimal by assembly into a hierarchical fractal arrangement. There are, however, few examples concerning the influence of geometrical pore assembly on catalyst effectiveness properties, although the importance of pore assembly architecture in determining the more complex issue of the speed of coke burn-off (hence rapidity of regeneration) in FCC catalyst particles has been demonstrated [32].

Hence the aim here is to explore catalyst support design issues, in order to enhance the transport of reactants to active sites and thereby minimise diffusional resistances for simple first order reaction. This approach amounts to the reorganization of the porosity to increase reactivity. In this respect it may well be possible to improve performance without resort to additional amounts of the usually expensive catalytic agent (often something like a precious metal), but by merely intelligently re-configuring the cost-free spaces that constitute the particle porosity [33].

6. Behaviour of a bimodal random pore network

6.1. Building a random network

Fig. 3(a) shows an illustrative 2D 30 × 30 idealised "square" pore network composed of 1860 (O(10^3)) pores obeying a bidisperse pore size distribution, with 50% by number of 0.12 μm diameter "small" pores and 50% 12 μm "large" pores. Subsequently we use a convenient shorthand, referring to small pores as micro-pores and large ones as macro-pores whilst noting clearly that this use is not in line with IUPAC definitions, where micro-pores are defined to be less than 2 nm (0.002 μm). The two classes of pores thus show a 100-fold difference in size (diameter). The random network shown in Fig. 3(a) is expected to be representative of many typical porous catalyst particles formed from the accretion of small micro-porous entities. The two sets of differently sized pores should be "shuffled" until well randomized and then allocated sequentially to build the network visualised. In this way the size of any pore is independent of the size of any neighbouring pores. Such pore assemblies are also referred to as stochastic pore networks.

6.2. Calculating a pore network concentration field

Reactivity is determined by solving the diffusion–reaction equation in every pore, to obtain the node concentrations throughout the network [18]. The boundary conditions are the external concentrations in the surrounding fluid to which the mouths of the outer set of pores are exposed. Then each and every individual pore in the network obeys the usual diffusion–reaction equation. The internal pore concentration profile can always be written in terms of the two adjacent node concentrations C' and C''. Using the fact that there must be a zero net flux (conservation) at all internal node points, gives a set of equations for all the node concentrations. This set of equations is linear for 1st order reaction and thus readily solved [18].

The consequent node concentration field for this random pore network is shown in Fig. 3(b) for a Thiele modulus value of 1.0 ($mL = 1$ using Levenspiel's terminology [34]) and an external concentration of 15 kmol m^{-3}. This Thiele modulus value reflects a moderate level of diffusional resistance. In a single equivalent uniform cylindrical pore, the dimensionless pore concentration would fall from 1 at the mouth to about 0.65 at the interior sealed end. For the network there is no sealed end, rather the composition will be minimised towards the centre of the network. However, it is immediately clear from Fig. 3(b) that the pattern of falling concentration towards the particle (network) centre is irregular, reflecting the random assembly of large and small pores. As a consequence, the concentration field for the nodes is quite "patchy", with some areas showing only a small departure from the outer boundary value of 15 kmol m^{-3}. In these regions the larger pores are locally predominant. Other localized areas however show significant node concentration reductions. This is a consequence of the combined effect of the higher specific surface offered where small pores happen to be more predominant (giving locally higher reactivity) plus the additional diffusional resistance to the fluxes caused by the reduced cross sectional areas available for transport by Fickian diffusion in the surrounding nearby small pores.

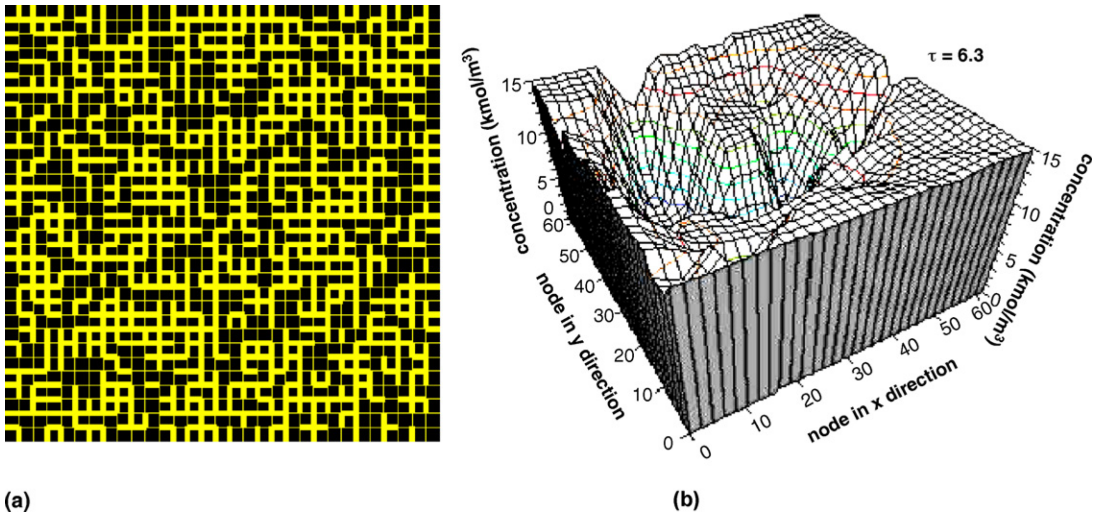

Fig. 3. Diffusion with reaction in a random bimodal pore network: (a) the random network; (b) concentration field in the network.

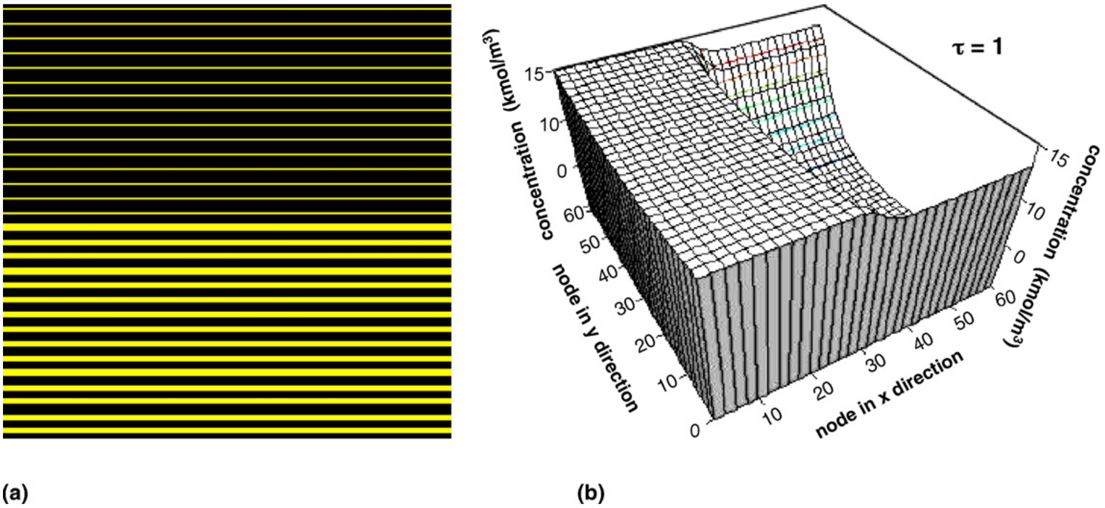

Fig. 4. Diffusion with reaction in the equivalent parallel bundle model: (a) the parallel bundle; (b) concentration field for the parallel bundle.

6.3. Behaviour of the equivalent parallel bundle

The bimodal network in Fig. 3(a) can be decomposed into the equivalent parallel bundle depicted in Fig. 4(a). The two sets of pores now appear distinctively with a length equal to the network (particle). In this equivalent assembly, the number of pore segments is identical so that the parallel bundle in Fig. 4(a) is comprised of exactly the same number of pore segments (1860). However the distinct difference in appearance arises because the pores are now no longer inter-connecting. Consequently there are two parallel bundles formed of 0.12 and 12 μm straight pores that do not intersect. Additionally, by building the individual segments into a parallel bundle, the impression of random corrugations as pores pass through the particle (network) now vanishes.

The corresponding node concentration fields for this equivalent parallel bundle at the same overall Thiele modulus of 1 ($mL = 1$) are displayed in Fig. 4(b). Because of the 100-fold difference in diameter, the large 12 μm pores in the parallel bundle show negligible reduction in concentration along their length. In contrast, the remaining much smaller pores exhibit a dramatic reduction, demonstrating that they suffer significant diffusional resistance when re-assembled into this baseline format.

6.4. Effectiveness of the random network

This random network is predicted to have effectiveness factors as shown in Fig. 5. It can be seen that the random assembly shows significantly lower effectiveness values than the equivalent parallel bundle. This is because many macropores in such a random network are in many locations (by chance) shielded behind micro-pores, resulting generally in lower levels of concentration within them. Because of this, the relatively large surface area in these pores offer less than their potential reactivity and their individual reaction effectiveness is lowered. In the mid range of Thiele modulus (around $mL = 1$), the random network has an effectiveness factor reduced to $\eta \approx 0.4$ corresponding to the (patchy) concentration field in Fig. 3(b). Whilst some parts of the 30 × 30 pore network show node concentrations close to 1.0, other parts exhibit large reductions falling towards zero. This ''patchy'' randomness in the concentration field is a result of the inherent randomness of the pore network.

6.5. Tortuosity as a measure of relative effectiveness

The procedure for calculating a tortuosity value for any given network (particle) is as described earlier [18] by Sharratt and Mann (1987). For a given pore network, for specified values of the surface rate constant k_s and diffusivity D, the overall network reaction rate and consequent effectiveness factor can be found as indicated above. From the computed value of effectiveness, the relevant value of an externally observed Thiele modulus Φ is derived by inverting the relationship

$$\eta = \frac{\tanh \Phi}{\Phi} = \frac{\tanh (m'L)}{m'L} \qquad (2)$$

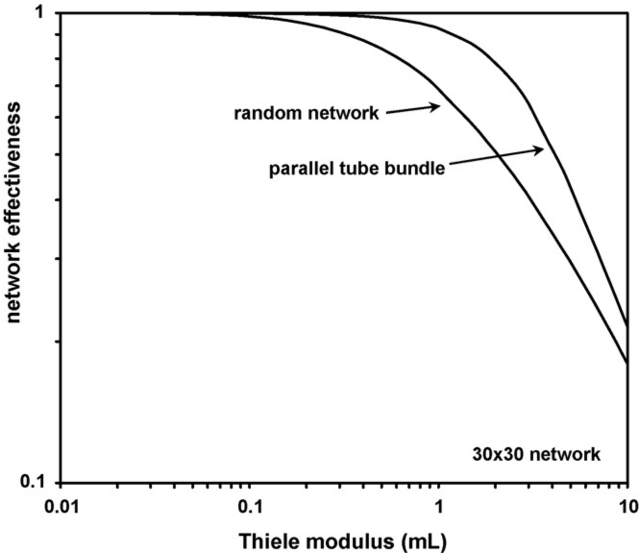

Fig. 5. Effectiveness factor for the random bimodal network.

The same approach to the parallel bundle thus provides values for $\Phi_{(\text{network})}$ and $\Phi_{(\text{parallel bundle})}$. Within these expressions are embedded the apparent (externally observed) values of the effective diffusivity for the pore network under consideration via the relationship

$$m'L = \left(\frac{2k_s}{rD_e}\right)^{1/2} L. \qquad (3)$$

Then from the definition of tortuosity in Eq. (1) and using a tortuosity of unity for the parallel bundle yields

$$\tau_{\text{network}} = \frac{(m'^2)_{\text{network}}}{(m'^2)_{\text{parallel bundle}}} \qquad (4)$$

The length terms cancel, since the network (particle) length is always the same in all cases.

The corresponding plot of tortuosity varying with intrinsic Thiele modulus is constructed by running the reactivity evaluations for variation of molecular diffusivity at fixed surface reaction rate constant.

The baseline unity value for tortuosity reflects the fact that when pores are formed into a parallel bundle, where all pores of a given size are perfectly straight, there is no deviation from straight-line paths for diffusion. Furthermore, large and small pores do not interact or interfere with each other in any way because they are completely non-inter-connected.

At a value for the network of m(L = 1, the tortuosity is 6.3. This value is indicated on the pictorialised node concentration field already depicted in Fig. 3(a). The plot of tortuosity versus Thiele modulus over five orders of magnitude is shown in Fig. 6. The apparent variation of tortuosity with Thiele modulus is grossly at variance with the concept that it should be a purely geometric property of the porosity. However, because Eq. (1) defines tortuosity only in relation to the apparent inferred value of D_e, it inevitably follows that under reaction conditions, it will paradoxically depend upon those elements related to reaction speed (here k_s) and molecular (or pore space) diffusivity, which of course have nothing to do with pore space geometry. This is then a consequence of deriving the effective diffusivity when reaction is present. Interestingly, this difficulty will not arise if the effective diffusivity is obtained solely from observations of non-reacting diffusional fluxes as in Wicke–Kallenbach experiments. However, tortuosity values are frequently reported for catalysts undergoing reaction.

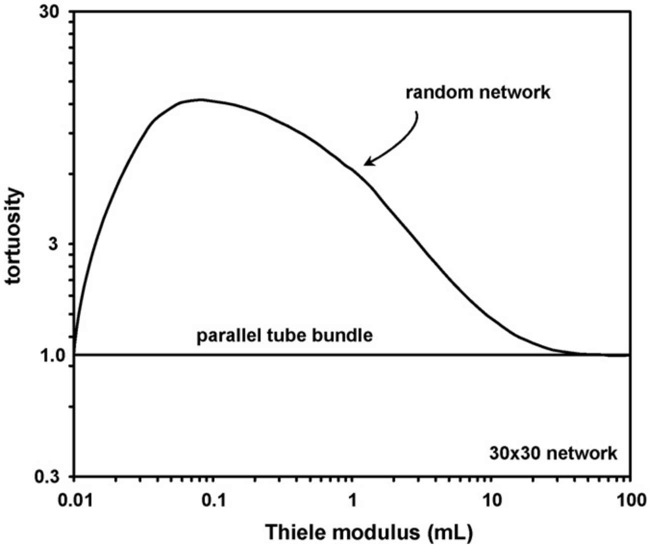

Fig. 6. Tortuosity factor for the random bimodal network.

6.6. Comparison via environmental distribution plots

The reaction performance as captured in Figs. 5 and 6 represents integration over the whole network. Underlying this comparison is the individual behaviour of each of the 1860 pore segments (half of which are macro-pores and half of which are micro-pores). This distributed behaviour can be examined via environmental frequency distribution plots of pore concentration versus pore size. These are depicted in Fig. 7 as 3D histograms, with vertical frequency ordinates, for the random and parallel bundle cases. The macro- and micro-pores form a pair of ‘‘walls’’ at each of the extremities of pore size in the perspective visualizations for the random network in Fig. 7(a). The vertical height represents the proportion of pores at each concentration. These are spread more or less uniformly for each of the pore sizes although there are peaks in concentration in both cases at each end (between zero and the external concentration) with troughs (lower frequencies) between. In the case of the micro-pores, the end frequencies are somewhat higher with the lower in-between frequencies then showing some gaps. For the parallel bundle, the pattern of behaviour of individual pores is noticeably different (as already apparent from the pictorialised concentration field in Fig. 4(b)). In this case the large macro-pores contain solely high concentrations contained in just two classes of the 15 element integer concentration distribution, hence none below 14 kmol m^{-3}, whereas the micro-pores are dominated by a median value at zero concentration. The effect of the network interconnectivity amongst pores of the two sizes is to smear out the concentrations between zero and the exterior value of 15 kmol m^{-3}. This behaviour is compactly captured in Fig. 7.

An additional degree of comparison can be included by colour/shade of grey coding each vertical histogram element. The colour code is shown at the head of Fig. 7 and uses gradations from ‘‘dark blue through light blue to colourless, continuing through light red to dark red’’ (or from ‘‘white through shades of grey to black’’) to illustrate how network pores are individually either less or more reactively efficient relative to the base parallel bundle case. The parallel bundle thus appears colourless (or a mid-grey shade using black and white) by comparison. Subsequently for different architectures, this style of representation means that the relative performance of alternative assemblies can be understood ‘‘at a glance’’ by observing the balance of red to blue (or white to black through grey) in the histogram. In the wholly random network shown here, this red/blue (or white/black) balance appears approximately evenly spread.

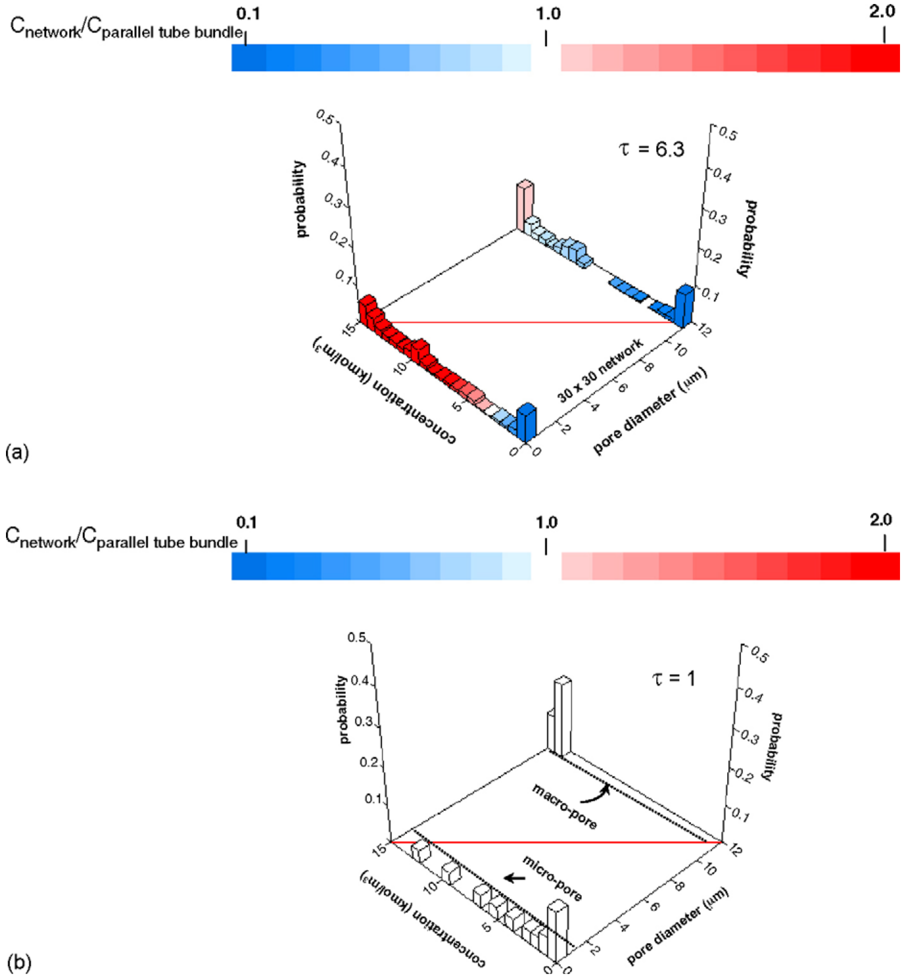

Fig. 7. Comparison of environmental distribution plots: (a) the random network; (b) the parallel bundle.

7. Behaviour of some re-assembled illustrative archetypes

7.1. Four illustrative archetype assemblies

If the dual-size set of pores in the random network (Fig. 3(a)) are fully disassembled, then rearranged and allocated into appropriate positions, the four illustrative pore architectures shown in Fig. 8(a)–(d) can be created.

In the minimum-shielding network shown as (a), all the large macro-pores are allocated to the network exterior and the small micro-pores to the interior. In this structure, the inner layer has the appearance of a denser solid. This configuration places all of the small micro-pores farthest from the network exterior, but provides for certainty that they will be able to be fed more efficiently through the surrounding set of larger diameter macro-pores.

When for the random network, a portion of the macro-pores are re-allocated to form a set of the larger cross pores aggregated through the centre, as shown in Fig. 8(b), this is called a partial cruciform configuration. In the example shown, the six central pores in both ‘‘vertical’’ and ‘‘horizontal’’ directions have had their small micro-pores exchanged with large macro-pores taken randomly from adjacent ‘‘quadrants’’. This results in improved diffusional access to the particle ‘‘centre’’ although some of the lateral-connecting small micro-pores remain in their previous positions within the cross-lines.

If the entire set of macro-pores are gathered together centrally, so as to form two orthogonal crossing sets now ten pores wide, as shown in Fig. 8(c), the two sets of macro-pores form a cruciform shape. In this case the large pores can ‘‘communicate’’ with each other overlapping perfectly all the way into the previously least accessible central region of the particle (network). The resulting four ‘‘square’’ smaller sub-networks of the entire solely smaller micro-pores created by this ‘‘fabrication’’ are then all nearer the external fluid (which supplies reagent for reaction) and are thereby less likely to experience the effects of diffusional limitations due to the smaller length scale of their sub-assembly and their proximity to the exterior bulk concentration.

Finally, the two sets of pore segments could be constructed into a sort of fractal tree or arterial leaf-like structural/architectural arrangement as portrayed in Fig. 8(d). In this assembly large pores branch deep into the centre of the network and provide large paths to communicate closely with virtually every remaining micro-pore. In this case, the inter-communication between large and small pores is significantly better than for the fully cruciform network, even though some of the

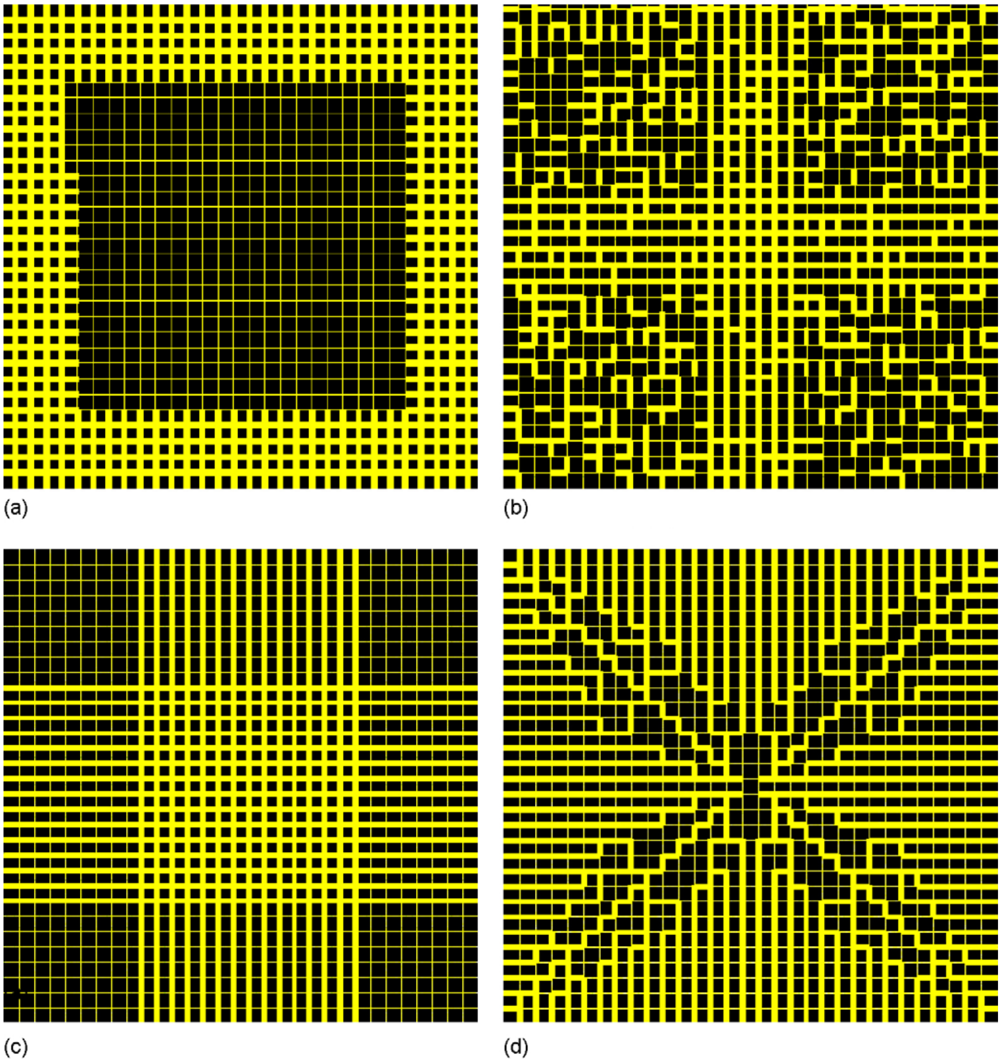

Fig. 8. Illustrative re-assembled archetypal pore networks: (a) minimum shielding; (b) partial cruciform; (c) fully cruciform; (d) fractal tree.

micro-pores lying buried deeper within the network might have been expected to consequently suffer a higher level of diffusional resistance.

7.2. Concentration fields for the illustrative archetypes

The set of concentration fields for the four archetypes are presented in Fig. 9 for $mL = 1$. For the minimum shielded network field in Fig. 9(a) there is negligible diffusional resistance in the outer macro-pores, although the interior micro-pores suffer sufficient diffusional resistance to substantially reduce the concentration towards the network centre. The overall effect however is to improve the reactivity and effectiveness by delivering a tortuosity factor of 0.8. Thus the integrated reaction performance of all the pores is 20% better than the parallel bundle and several factors better (8×) than the corresponding random case.

It is also immediately evident from Fig. 9(b) that the re-arrangement of the bimodal set of pores into the partial cruciform results in improved reaction performance. This can be seen from the relatively higher concentrations that the re-assembly delivers towards the centre of the network by virtue of the preferential increase in proportion of larger macro-pores within the centrally configured six-row pairs orthogonally intersecting vertically and horizontally. This rearrangement also delivers an increased proportion of smaller pores towards the outside of the network, placing them closer to the high level exterior concentration ‘‘bathing’’ the network. The integrated performance here gives a tortuosity factor of 4.3, which is an approximately 25% improvement on the random network case.

Re-assembly into the full cruciform configuration delivers further improvement in reactivity as is immediately evident from the field shown in Fig. 9(c). The orthogonal pair of crossing macro-pores means that the centre of the particle actually ‘‘sees’’ the external concentration. The four corner smaller sub-assemblies of micro-pores experience a reduced level of diffusional resistance, which in aggregate is lower than in Fig. 9(b) and (c). The overall effect produces a tortuosity factor below 1 at 0.97, thus better than the parallel bundle.

Finally the improvement from the fractal tree architecture is very striking as can be seen by inspecting the node

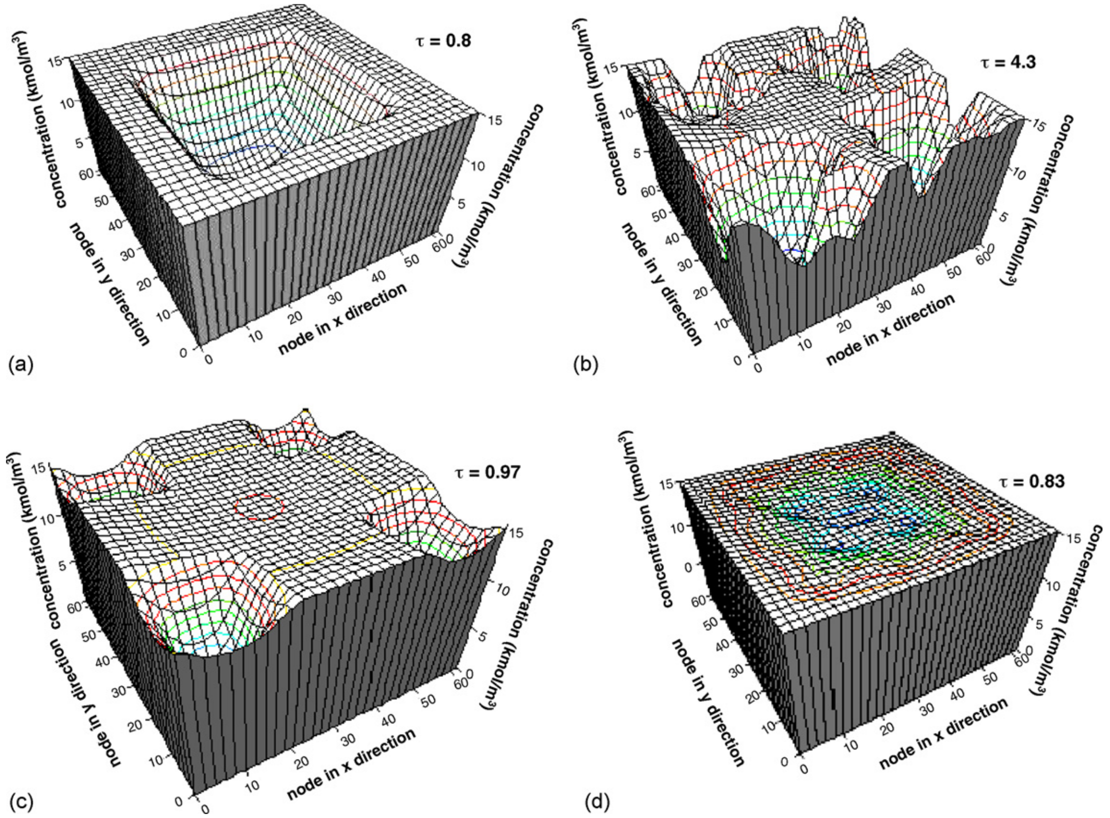

Fig. 9. Node concentration fields at $mL = 1$ for illustrative archetypes: (a) minimum shielding; (b) partial cruciform; (c) fully cruciform; (d) fractal tree.

concentration field pictorialised in Fig. 9(d). For the branching tree network in Fig. 9(d), macro-pores branch out, so that they inter-penetrate and are inter-connected into all parts of the whole network. It is obvious that this configuration improves the diffusive access to such an extent that all the dimensionless node concentrations now become everywhere very close to 1. Surprisingly, the node concentration field in the branching tree in Fig. 9(d) whilst showing this significant gain in uniform node concentrations throughout the network, avoids the greater gradients of concentration in the minimum shielding network in Fig. 9(a). As is obvious by inspection, all the nodes have concentrations very close to the exterior value. The tortuosity factor for this assembly is 0.83. This value of less than unity shows that inter-connectivity and assembly architecture can render a reactivity that is higher than produced by having pores that are straight and of uniform diameter and length. Notice that this sub-unity tortuosity value means that the fractal tree network is predicted to be some eight times more reactive than its random counterpart. Such an 800% enhancement in reactivity is all the more remarkable if we recognise that this has been achieved only by re-arranging the pore spaces. Consider how much more expensive it would be to try and produce this degree of reaction improvement using, say, a precious metal catalyst like platinum.

7.3. Effectiveness factors and tortuosity behaviour

Fig. 10 shows the effectiveness factor plots for the four re-assembly archetypes. In line with the qualitative appreciation of behaviour from the node concentration field described above, the relative positioning of each archetype on theses plots more or less reflects the tortuosity values. Over the whole range of Thiele modulus values, the minimum shielding case is always superior, giving rise to tortuosity values less than unity as depicted in Fig. 11. The lowest tortuosity value is at approximately 0.2 at $mL = 5$, after decreasing from unity at very low values of mL. The fractal tree case asymptotes to a lowest value of 0.25, as the Thiele modulus increases towards 100. The fully cruciform case is close to 1.0 throughout the range from $mL = 0.01$ to 100,

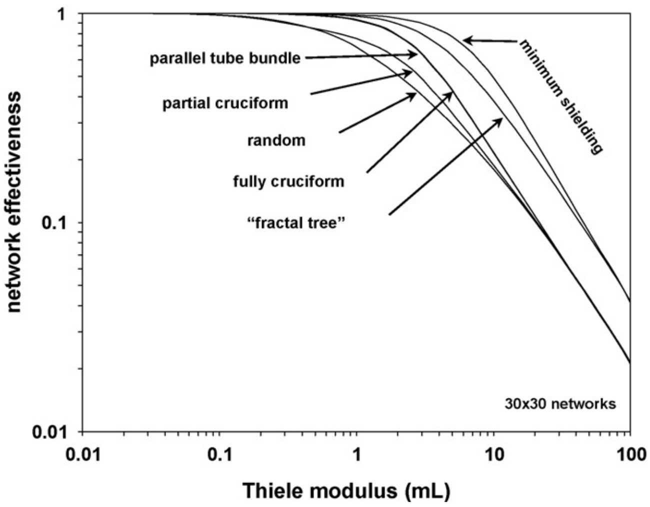

Fig. 10. Effectiveness factors for the four archetypes.

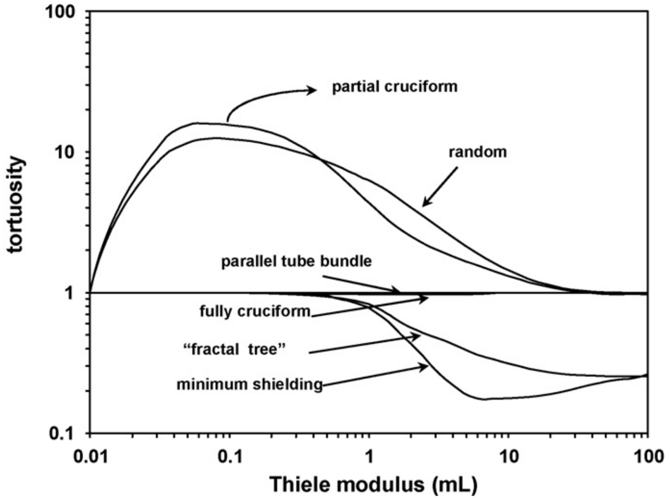

Fig. 11. Tortuosity factors for the four archetypes.

which would reflect a ten thousand fold variation in catalytic reactivity. The partial cruciform case is initially superior to the random network at lower *mL* values, but beyond $mL = 0.5$, the random example is slightly superior.

It is interesting to note that the tortuosity values in Fig. 11 more or less span the range of values observed experimentally (e.g. Satterfield (1980) quotes values between 0.6 and 6). Also of particular interest is that it is quite feasible for the overall architecture to sensibly exhibit values less than unity, depending upon the inter-connectivity and layout of the pores when referenced to a parallel bundle. This is relevant to deductions of pore size distribution via nitrogen adsorption/capillary condensation isotherms that, because there is no effect of inter-connectivity or accessibility, intrinsically would yield the parallel bundle distribution.

7.4. Comparison via environmental distribution plots

The corresponding four environmental distribution plots are shown in Fig. 12. These plots show the detail of the improved diffusion/reaction behaviour already identified from the integrated effectiveness factor values. This is further revealed at a glance because of the colour coding (black/grey/white shading). Those pores showing dark red (fully black) are at least twice as reactive (they possess a concentration at least two times greater and the reaction is first order) than they were in

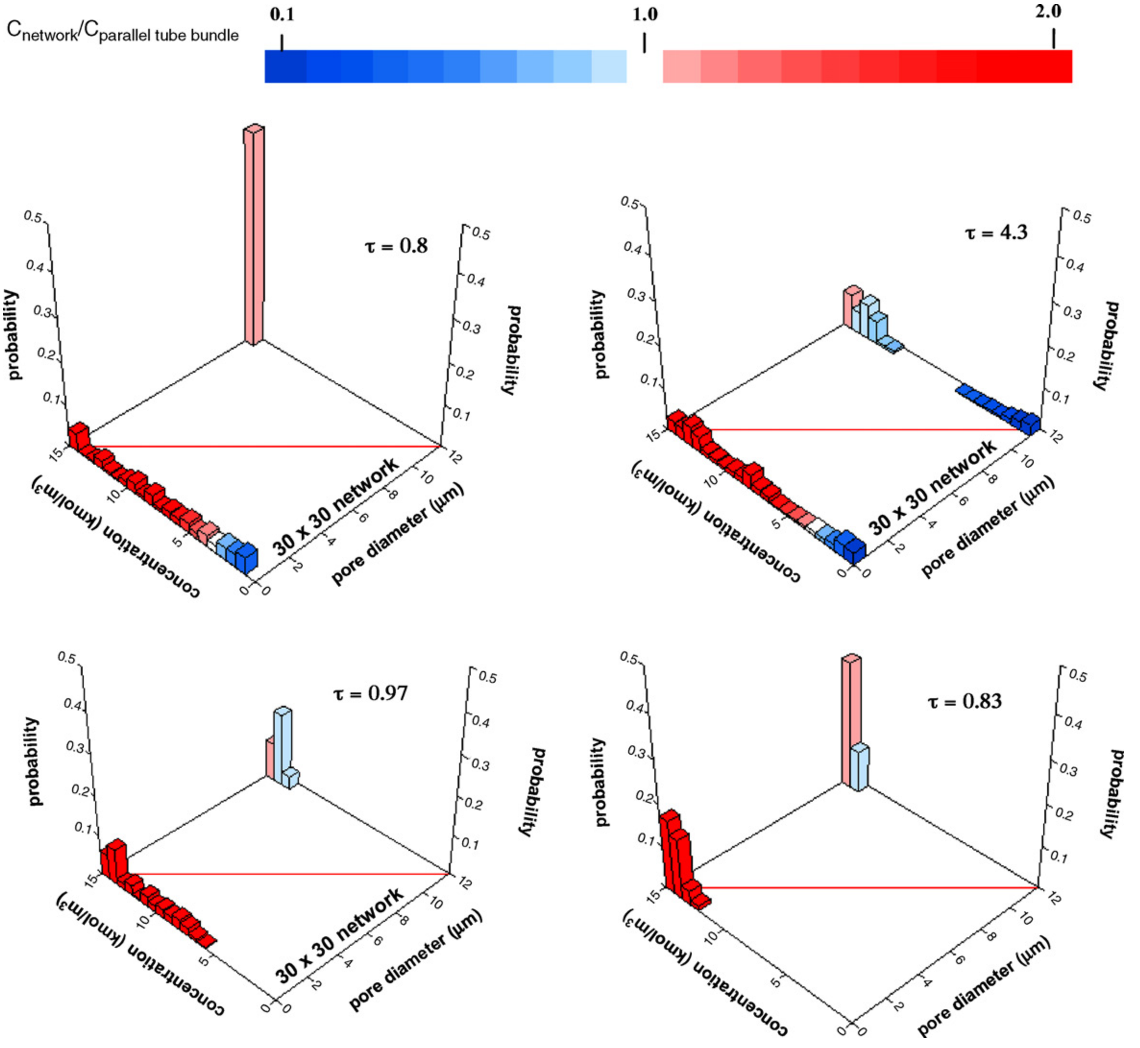

Fig. 12. Environmental distributions for illustrative archetypes: (a) minimum shielding; (b) partial cruciform; (c) fully cruciform; (d) fractal tree.

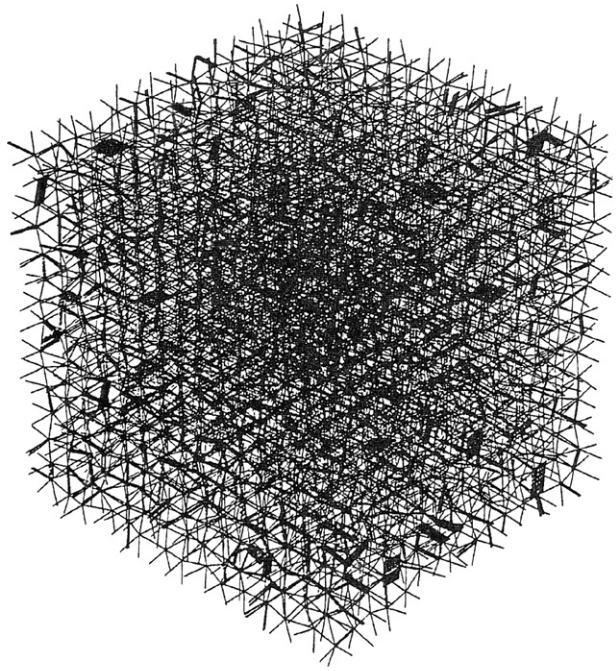

Fig. 13. A 3D pore network of size 15 × 15 × 15 with random diameter and random length pores.

the parallel bundle. All four cases in Fig. 12 show a very large proportion of the small micro-pores are deep red (black). There are only a few pores showing blue (white or light grey) for these micro-pores in the minimum shielding (a) and partial cruciform (b). For the fully cruciform case (c) and the fractal tree (d) all the micro-pores without exception outperform the parallel bundle case. The re-structuring of the large macro-pores has facilitated better transport to these micro-pores by providing more large diameter uninterrupted pathways to them. For the macro-pores, in case (a) they all show significant improvement (seen from the pale red colour or dark grey) and none experience concentrations lying below 14 kmol m^{-3}. For the partial cruciform in (b), the micro-pore performance is just slightly worse than for case (a), but the macro-pores show a much decreased performance with a large proportion coloured dark blue or close to white/very light grey (up to 10 times worser than the parallel bundle) with concentrations lying between 5 kmol m^{-3} and zero. However, the overall performance is an improvement with a tortuosity value for this assembly of 4.3. For the fully cruciform layout in (c), all the dark blue (white/light grey) vertical ordinates have been entirely eliminated for both the macro- and micro-pores, thus showing how pores of different sizes contribute to the improved lower tortuosity value of 0.97. Finally, in (d) for the fractal tree, a further improvement in tortuosity down to 0.83 is reflected in the deep red colour (black) of the micro-pore ordinates as well as the increase of the lowest concentration to 12 kmol m^{-3}, whilst the macro-pores show improvements as pale red (darker grey) and pale blue (light grey) with now no concentrations below 12 kmol m^{-3} for the full cruciform and none below 13 for the fractal tree.

8. Conclusions

- Our understanding of the role of the structural complexities of catalyst particle porosity and morphology, as readily revealed by SEM images up to 2000× magnification, is still very limited.
- Simple 2D pore networks comprised of cylindrical pore segments with $O(10^3)$ elements have been successfully used to examine variations in the assembly architecture and the consequences for diffusion and reaction with first order surface catalysed reaction. Results have been presented for the special bimodal pore size distribution case with equal numbers of single sized micro-pores and macro-pores, expected to be illustrative of real catalyst particles fabricated from smaller micro-porous particles.
- Referring such pore networks to the equivalent parallel bundle model allows prediction of a tortuosity value from first principles, albeit for a simplified model of particle porosity.
- It has been demonstrated that the same porosity re-assembled into different architectures will exhibit radically different reactivity/catalyst effectiveness performance, even though the pore volume and specific surface remain identical.
- The random network forms a useful baseline comparator in which the micro- and macro-pores are spatially randomly allocated. At a Thiele modulus (mL) of 1, this base case has a relatively high tortuosity of 6.3.
- Four illustrative architectures have been appraised—referred to as minimum shielding, partial cruciform, full cruciform and fractal tree.
- At $mL = 1$, the tortuosity values are predicted to be 0.8, 0.83, 4.3 and 0.97, respectively. The highest reactivity at the lowest tortuosity for minimum shielding is thus some 800% more reactive than for the random network case. The values less than unity show how large macro-pores can be beneficially arranged to improve diffusional access to the micro-pores, so that overall even the parallel bundle with perfectly straight uniform pores can be improved upon.

Colour coded (grey shaded) concentration environment plots help to reveal the detail of the improvements in diffusion reaction performance.

These illustrations need to be extended to more realistic 3D networks as in Fig. 13. The potentially more practical improvements predicted from 3D should provide a motivation to explore the bigger question of optimal pore assembly architectures for a specific porosity, to include extension to the more practical cases of multi-component diffusion and reaction.

References

[1] R. Aris, Elementary Chemical Reactor Analysis, Prentice Hall Englewood Cliffs, NJ, 1969.

[2] C.N. Satterfield, Heterogeneous Catalysis in Practise, McGraw-Hill, New York, 1980.

[3] G.F. Froment, K.B. Bischoff, Chemical Reactor Analysis and Design, Wiley, New York, 1990.

[4] R. Hughes, Deactivation of Catalysts, Academic Press, London, 1984.

[5] H. Scott Fogler, Elements of Chemical Reaction Engineering, 3rd ed., Prentice Hall PTR, New Jersey, 1992.

[6] E.B. Nauman, Chemical Reactor Design, Optimisation and Scale-Up, McGraw-Hill, New York, 2002.

[7] I. Chorkendorff, J.W. Niemantsverdriet, Concepts of Modern Catalysis and Kinetics, WILEY-VCH Verlag GmbH, Weinheim, 2003.

[8] A. Wheeler, Reaction rates and selectivity in catalyst pores, Adv. Catal. 3 (1951) 249.

[9] B. Sapoval, J.S. Andrade, M. Filoche, Catalytic effectiveness of irregular interfaces and rough pores: the land surveyor approximation, Chem. Eng. Sci. 56 (2001) 5011.

[10] M.C. Wasilewski, R. Mann, Towards a fractal computer graphic basis for pore structure characterisation by image reconstruction, ChERD 68(A) (1990) 177.

[11] K. Malek, M.-O. Coppens, Knudsen self- and Fickian diffusion in rough nanoporous media, J. Chem. Phys. 119 (2003) 2801.

[12] D.B. Bukur, X. Lang, D. Mukesh, W.H. Zimmerman, M.P. Rosnyek, C. Li, Binder/support effects on the activity and selectivity of iron catalysts in the Fischer–Tropsch synthesis, Ind. Eng. Chem. Res. 29 (1990) 1588.

[13] L.D. Sharma, M. Kumar, A.K. Saxena, M. Chand, J.K. Gupta, Influence of pore size distribution on Pt dispersion in Pt–Sn/Al_2O_3 reforming catalyst, J. Mol. Cat. A-Chem. 185 (2002) 135.

[14] B. RaviKumar, Effect of silica support on V–Mg–O catalysts during ODH of propane: experimental and modelling using genetic algorithms, Int. J. Chem. React. Eng. 4 (2006) A28.

[15] L. Mercier, T.J. Pinnavaia, Access in mesoporous materials: advantages of a uniform pore structure in the design of a heavy metal ion adsorbent for environmental remediation, Adv. Mater. 9 (1997) 500.

[16] G.P. Androutsopoulos, R. Mann, Evaluation of mercury porosimeter experiments using a network pore structure model, Chem. Eng. Sci. 34 (1979) 1203.

[17] R.L. Portsmouth, L.F. Gladden, Determination of pore connectivity by mercury porosimetry, Chem. Eng. Sci. 46 (1991) 3023.

[18] P.N. Sharratt, R. Mann, Some observations on the variation of tortuosity with Thiele modulus and pore size distribution, Chem. Eng. Sci. 42 (**7**) (1987) 1565.

[19] M.P. Hollewand, L.F. Gladden, Modelling of diffusion and reaction in porous catalysts using a random three-dimensional network model, Chem. Eng. Sci. 47 (1992) 1761.

[20] F. Wang, X. Feng, S. Li, A random network model for spherical porous catalyst, J. Chem. Ind. Eng. 50 (3) (1999) 309.

[21] S.P. Rigby, M.J. Watt-Smith, R.S. Fletcher, Simultaneous determination of the pore length distribution and pore connectivity for porous catalyst supports using integrated nitrogen sorption and mercury porosimetry, J. Catal. 227 (1) (2004) 68.

[22] C. Rieckmann, F.J. Kiel, Multicomponent diffusion and reaction in three dimensional networks: general kinetics, Ind. Eng. Chem. Res. 36 (1997) 3275.

[23] C. Rieckmann, F.J. Kiel, Simulation and experiment of multicomponent diffusion and reaction in three dimensional networks, Chem. Eng. Sci. 54 (1999) 3485.

[24] V. Popescu, C. Oprea, S. Birghila, Multicomponent diffusion and reaction in three-dimensional networks, J. Optoelectron. Adv. Mater. 5 (2003) 1439.

[25] J. Wood, L.F. Gladden, F.J. Keil, Modelling diffusion and reaction accompanied by capillary condensation using three dimensional pore networks, Chem. Eng. Sci. 57 (2002) 3047.

[26] E.S. Kikkinides, A.S. Lappas, A. Nalbadian, I.A. Vasalos, Correlation of reactor performance with catalyst structural changes during coke formation in FCC processes, Chem. Eng. Sci. 57 (2002) 1011.

[27] C. Mhas, A.D. Araujo, H.F. da Silva, J.S. Andrade Jr., Scaling behaviour of diffusion and reaction processes in percolating porous media, Phys. Rev. E 67 (2003) 061406.

[28] J.M. Zalc, S.B. Reyes, E. Iglesia, Monte-Carlo simulations of surface and gas phase diffusion in complex porous structures, Chem. Eng. Sci. 58 (2003) 4605.

[29] J.M. Zalc, S.B. Reyes, E. Iglesia, The effects of diffusion mechanism and void structure on transport rates and tortuosity factors in complex pore structures, Chem. Eng. Sci. 59 (2004) 2947.

[30] F.J. Keil, C. Rieckmann, Optimisation of three-dimensional catalyst pore structures, Chem. Eng. Sci. 49 (1994) 4811.

[31] S. Gheorgiu, M.-O. Coppens, Optimal bimodal pore networks for heterogeneous catalysis, AIChEJl 50 (4) (2004) 812.

[32] U.A. El-Nafaty, R. Mann, Support-pore architecture optimisation in FCC catalyst particles using designed pore networks, Chem. Eng. Sci. 54 (1999) 3475.

[33] S. Prachayawarakorn, Designing efficient pore architectures for catalyst particles', PhD Thesis, UMIST (2000).

[34] O. Levenspiel, Chemical Reaction Engineering, 3rd ed., John Wiley & Sons, New York, 1999.